Computationally driven discovery of a family of layered LiNiB polymorphs

Computationally-driven discovery of the family of layered LiNiB polymorphs

Volodymyr Gvozdetskyi,[a] Gourab Bhaskar,[a] Maria Batuk,[b] Xin Zhao,[c] Renhai Wang,[d] Scott L. Carnahan,[a], [c] Michael P. Hanrahan,[a], [c] Raquel A. Ribeiro,[c], [e] Paul C. Canfield,[c], [f] Aaron J. Rossini, [a], [c] Cai-Zhuang Wang,[c] Kai-Ming Ho,[c], [g],[f], Joke Hadermann,[b] and Julia V. Zaikina*[a]

Abstract: Two novel lithium nickel boride polymorphs *RT*-LiNiB and *HT*-LiNiB with layered crystal structures are reported. This family of compounds was theoretically predicted by using the adaptive genetic algorithm (AGA) and subsequently synthesized via a hydride route with LiH precursor as a lithium source. Being unique among the known ternary transition metal borides, the LiNiB structures feature Li layers alternating with nearly planar [NiB] layers, composed of Ni hexagonal rings centered by B-B pairs. A comprehensive study using a combination of single crystal/synchrotron powder X-ray diffraction data, solid-state ^{7}Li and ^{11}B NMR, scanning transmission electron microscopy, quantum chemistry calculations, and magnetism has shed light on the intrinsic features of these polymorphic compounds. The unique layered structures of LiNiB compounds make them ultimate precursors to further study their exfoliation, paving a way toward two-dimensional transition metal borides, MBenes.

Introduction

The crystal structure prediction of ternary or multinary inorganic materials is a challenging task given the diversity of the potential structures.[1,2] Yet, the experimental validation of the computational predictions is a vital step for the accelerated materials discovery and further strengthening the predictive power of the computational methods.[1a],[1c] Solid state chemistry synthetic routes lack the predictability of the synthesis outcome,[8] compared to organic chemistry synthesis, where the molecular units can be linked to form the target product, followed by the specific modifications of the functional groups. Yet, the theoretical predictions of structure and thermodynamic stability of the new ternary phases can yield the desired roadmap for the targeted exploration of ternary systems.[3] On the other hand, efficient synthetic experimental approaches allow for the fast screening of the compositional space, allowing for the rapid phase discovery and timely feedback for the iterative improvement of theoretical predictions.[3]

From the functional materials perspective, class of transition metal borides showcases a variety of structural frameworks and broad range of their properties and applications.[4] Sparked by the successful preparation and unique properties of the two-dimensional (2D) transition metal carbides (named MXene),[5] the search 2D borides (MBene) has launched. Computational predictions point out to the stability and potential intriguing properties of 2D transition metal borides, such as enhanced ferromagnetic Curie temperatures for spintronics, superior catalytic activity for the hydrogen evolution reaction, high storage capacity for Li ion batteries, flexibility, high specific surface area, and quasi-2D electron confinement.[6] The synthesis and experimental validation of these computational predictions have yet to be realized. To the best of our knowledge, the experimental reports about synthesis of MBene are limited to the three examples.[7] Borophane sheets were obtained by exfoliation of layered MgB_2 superconductor,[7a] while topochemical deintercalation of Al from MoAlB yields 2D MoB.[7b] The most recent example is preparation of a layered boride TiB by the removal of the indium layer from the parent Ti_2InB_2.[7c]

The exfoliation of highly labile alkali metal cations, such as Li^+, Na^+, K^+, from the layered structures of the alkali-transition metals borides *A*-*T*-B (*A* = alkali metal, *T* = transition metal group 4-12) could be a facile route toward the stable 2D [*T*B] architectures, provided that suitable layered precursors are identified among those scarcely studied *A*-*T*-B systems. Alkali metal borides hold certain synthetic challenge. In contrast to the over 800 *RE*-*T*-*B* phases (*RE* = rare earth element, *T* = transition metal group 4-12) which show a rich variation in their crystal chemistry,[8] composition, transport and magnetic properties only 16 phases are known in 160 possible different *A*-*T*-B ternary systems and only 3 ternary compounds containing 3*d* metals (V-Ni) were known so far, all of them in the Li-Ni-B system.[9] Synthesis of *A*-*T*-B ternary systems is challenging because the ductility of the elemental alkali metals precursors makes it difficult to

[a] Dr. V. Gvozdetskyi, G. Bhaskar, S.L. Carnahan, M.P. Hanrahan, Prof. Dr. A.J. Rossini, Prof. Dr. J.V. Zaikina*
Department of Chemistry
Iowa State University
Ames, Iowa 50011, United States
E-mail: yzaikina@iastate.edu

[b] Dr. M. Batuk, Prof. Dr. J. Hadermann
EMAT, Department of Physics
University of Antwerp
Antwerp 2020, Belgium

[c] Dr. X. Zhao, S.L. Carnahan, M.P. Hanrahan, Dr. R.A. Ribeiro, Prof. Dr. P.C. Canfield, Prof. Dr. A.J. Rossini, Dr. C.-Z. Wang, Prof. Dr. K.-M. Ho
Ames Laboratory
US DOE, Iowa State University
Ames, Iowa 50011, United States

[d] R. Wang, Prof. Dr. K.-M. Ho
Department of Physics
University of Science and Technology of China
Hefei 230026, China

[e] Dr. R.A. Ribeiro
CCNH
Universidade Federal do ABC (UFABC)
Santo André, SP 09210-580, Brazil

[f] Prof. Dr. P.C. Canfield, Prof. Dr. K.-M. Ho
Department of Physics and Astronomy
Iowa State University
Ames, Iowa 50011, United States

Supporting information for this article is given via a link at the end of the document.

homogeneously mix the components of the reaction mixture. Previously, we have utilized alkali metal hydrides *A*H (*A* = Li, Na, K) as mixable salt-like precursors for the fast experimental exploration of ternary systems, containing alkali metals.[10,11a,11b] The hydrides precursors remedy mixing issues leading to the faster reactions.[10-11]

Here, we are reporting the computationally driven experimental discovery of two polymorphs of the novel transition metal boride LiNiB with unique layered crystal structure. By using an adaptive genetic algorithm (AGA) for *ab initio* prediction of crystal structure,[2], [12] and facile synthesis route using lithium hydride precursors, two polymorphs of the novel layered LiNiB have been identified. Insights about their unique crystal and electronic structures are provided by advanced characterization methods, including single crystal and synchrotron powder X-ray diffraction, scanning transmission electron microscopy (STEM), ^{7}Li and ^{11}B solid-state NMR, and magnetic properties. These layered LiNiB compounds are suitable precursors for further exfoliation and modification via soft chemistry routes to access 2D [NiB] layers.

Results and Discussion

Calculated thermodynamic stability, structure prediction, and synthesis. The exploration of the ternary Li-Ni-B system was started by calculating the energies of all of the previously reported binary and ternary phases[9], [10] (Figure 1). Here all stable compounds are represented by solid red triangles and metastable phases with formation energies above the convex hull are represented by hollow blue triangles. Besides the experimentally discovered and characterized $LiNi_3B_{1.8}$, $Li_{2.8}Ni_{16}B_8$, and $Li_3Ni_{20}B_6$ phases,[9,10] the equiatomic LiNiB compound was predicted to be stable. The possible existence of the compound with the composition similar to LiNiB was pointed out in the earlier publication by *Jung*,[9a] but no crystal structure was reported. From the adaptive genetic algorithm (AGA) searches[2,12] for the structure of LiNiB compound, the lowest energy structure was found in space group $P2_1/c$ (a = 4.57511 Å, b = 4.82613 Å; c = 6.12969 Å, β = 109.4064°), which was subsequently confirmed experimentally as *RT(m)*-LiNiB.

The thermodynamic stability of *RT(m)*-LiNiB can be determined by the Gibbs triangle formed by $LiNi_3B_2$, LiB, and Li (Figure 1*a*), considering the following reaction: $3LiNiB \rightarrow LiNi_3B_2 + LiB + Li$. DFT calculations show that the formation energy of *RT(m)*-LiNiB is equal to -339 meV/atom, while the energy on the convex hull at the composition of LiNiB, is -269 meV/atom. Therefore, *RT(m)*-LiNiB is thermodynamically stable at 0 K and the convex hull of the Li-Ni-B system can be updated (Figure 1*b*) with the inclusion of a newly predicted ternary phase.

Following the computational input, the sample of *RT*-LiNiB was synthesized via hydride route from LiH, Ni and B. We have shown previously[10] that this route is feasible for the preparation of previously reported ternary lithium nickel borides using a mixable LiH precursor. In the case of the $LiNi_3B_{1.8}$ phase this route is considerably faster, as compared to the elemental Li metal precursor route (20 h annealing vs. 90 days annealing).[10] The high-temperature polymorph *HT*-LiNiB was prepared by quickly removing the reaction vessels at 1173 K from the furnace and immersing them into cold water. Quenching from 973 K and 1073 K yields only *RT*-LiNiB, indicating that *HT*-LiNiB is stable above ~ 1173 K. For the synthesis of both *RT*-LiNiB and *HT*-LiNiB, an excess of lithium hydride and boron was found to be necessary. LiH:Ni:B molar ratios of 1.3:1:1.15 featuring a minimal excess of LiH and B (experimentally determined) were required to obtain phase pure samples.

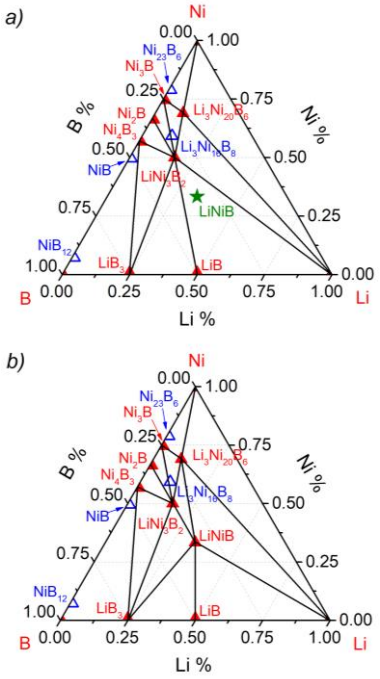

Figure 1. Calculated convex hull of the formation energies in the Li-Ni-B system: a) based on previously reported phases, b) after including the newly discovered *RT(m)*-LiNiB phase. All calculations were carried out at 0 K. Red solid triangles represent stable compounds, while blue hollow triangles indicate the metastable phases. The black lines separate the composition space to Gibbs triangles.

Synthesis from the elements was also carried out. This method resulted in samples containing LiNiB compounds thus confirming that hydrogen is not involved in the structure stabilization. However, the products of the elements reactions were found to be inhomogeneous, less crystalline, and contained impurities of $LiNi_3B_{1.8}$ and $Li_{2.8}Ni_{16}B_8$ phases (Figure S1).

Crystal structure determination. Crystals of *RT*-LiNiB and *HT*-LiNiB were extensively twinned with broad reflections, making accurate SC XRD analysis complicated. The diffraction patterns of LiNiB phases are dominated by the contribution from heavy Ni atoms, thus enabling determination at least basic structure motifs from the low-quality SC XRD data.

For the *RT*-LiNiB phase two types of single crystals were found: the majority of the crystals revealed a monoclinic unit cell (a = 4.587(2) Å, b = 4.822(2) Å, c = 6.153(3) Å, β = 109.71(2)°, V = 128.1(1) Å^3). This unit cell (hereinafter referred to as *RT(m)*-LiNiB) is the same unit cell as determined from the adaptive genetic algorithm (AGA) crystal search, as well as from indexing of synchrotron powder XRD data. Because of considerable twinning refinement of the crystal structure was not possible. A minor

amount of crystals, albeit better diffracting, were found to crystalize in the $Cmc2_1$ space group with the doubled unit cell volume as compared to *RT(m)*-LiNiB (a = 4.8177(7) Å, b = 6.1421(9) Å, c = 8.641(1) Å, V = 255.68(7) Å^3, hereinafter referred to as *RT(o)*-LiNiB) (Table S1 and S2).

Crystals of the *HT*-LiNiB phase were indexed in the monoclinic $P2_1/m$ space group (a = 3.91012 Å, b = 8.8099 Å, c = 7.5240 Å, β = 90.070°, V = 259.19 Å^3). The structure of the [NiB] layer was determined, while the positions of the Li atoms in the interlayer space were further obtained from synchrotron PXRD data as well as from DFT-guided optimization of Li atomic coordinates for the fixed Ni and B coordinates within the [NiB] layer. Crystallographic parameters and results of Rietveld refinements of synchrotron X-ray diffraction data are listed in Tables S3-S8, Figures S2-S4.

Both *RT*-LiNiB and its high-temperature polymorph *HT*-LiNiB have a common structure motif, that is [NiB] layers alternating with Li layers. As a result, their PXRD patterns are similar (Figure 2): the most intense diffraction peak at ~4.34-4.41 Å corresponds to the interlayer distance between [NiB layers] (highlighted in yellow, Fig. 2), while the rest of the PXRD patterns differ (highlighted in blue, Fig. 2), indicating the difference in the atomic arrangement within the [NiB] layer and Li atoms between the layers.

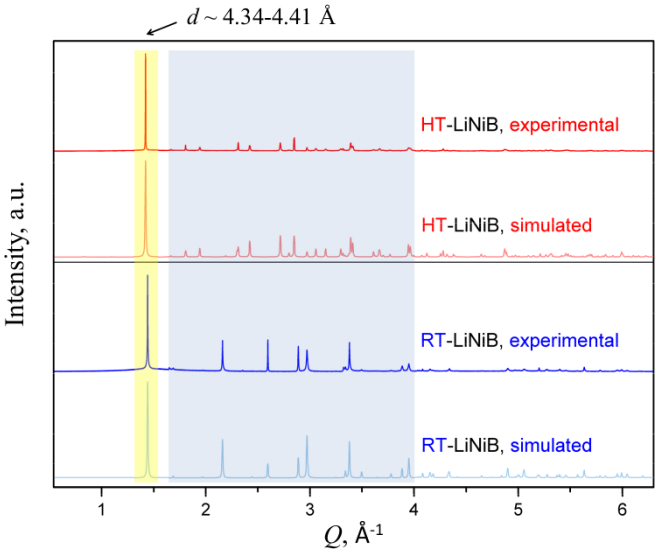

Figure 2. Experimental synchrotron powder X-ray diffraction patterns of *RT*-LiNiB and *HT*-LiNiB shown together with relevant simulated patterns from derived experimentally derived structures (*RT(m)*-LiNiB and *HT*-LiNiB). The most intense characteristic peak d ~ 4.34-4.41 Å (highlighted in yellow) corresponds to the distance between [NiB] layers. This peak is common for both phases, which however have different atomic arrangement within the [NiB] layers, as indicated by the differences in the blue-shadowed region. The simulated PXRD patterns were calculated for the crystal structures of *RT(m)*-LiNiB and *HT*-LiNiB obtained by solving structures using synchrotron PXRD.

Indexing of the high-resolution synchrotron powder X-ray diffraction data (PXRD) with the program FOX[13] gave the same unit cell and symmetry for *RT*-LiNiB phase, as those determined by SC XRD and adaptive genetic algorithm (AGA) crystal search (*RT(m)*-LiNiB) (Figure S2, Table S3-S5). Similarly, for the high temperature polymorph *HT*-LiNiB indexing of the synchrotron PXRD data led to the same unit cell as that determined from SC XRD (Figure S4, Table S3, S6). Structures of all LiNiB phases were solved from synchrotron PXRD data.

Interestingly, the experimental PXRD pattern of the *RT*-LiNiB compound can be described as a "combination" of both *RT(m)*-LiNiB and ($P2_1/c$) and *RT(o)*-LiNiB ($Cmc2_1$) with the refined ratio of 89.6(4):10.4(4) (Figure S5). These two structures differ in the stacking sequence of [NiB] layers, suggesting that the structure of *RT*-LiNiB compound is complex intergrowth of the different stacking sequence of [NiB] layers. Alternatively, superstructure of *RT(m)*-LiNiB ($P2_1$/c) with 4-fold enlargement of *a*-parameter allows to describe most of the peaks at PXRD pattern, but still does not reflect accurately the real crystal structure (Table S9, Figure S6). This superstructure includes features of both *RT(m)*-LiNiB and *RT(o)*-LiNiB polytypes. Similarly, high resolution synchrotron powder X-ray data of *HT*-LiNiB compound reveal splitting of several peaks corresponding to corresponding to hkl families (020), (040), (060), (080), (002), (006), indicating on even more complicated superstructure (Figure S7).

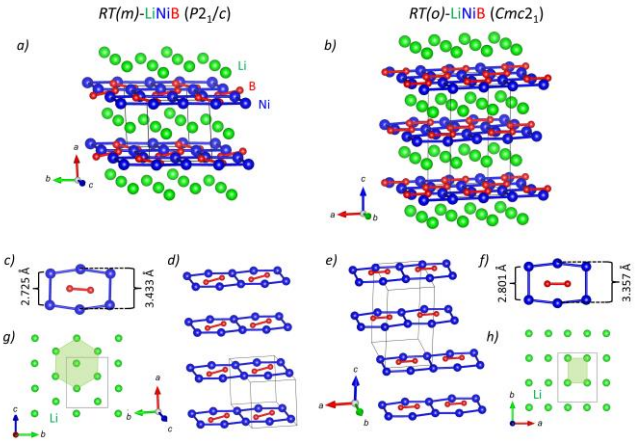

Figure 3. Crystal structures of *a*) *RT(m)*-LiNiB and *b*) *RT(o)*-LiNiB. Structures are built from Ni_6B_2 units with different interatomic Ni-Ni distances: c) *RT(m)*-LiNiB and *f*) *RT(o)*-LiNiB; *d*) stacking of [NiB] layers in *RT(m)*-LiNiB and *e*) in *RT(o)*-LiNiB; Li layers in *g*) *RT(m)*-LiNiB and h) *RT(o)*-LiNiB.

Layered structures relationship. The crystal structures of *RT(m)*-LiNiB and *RT(o)*-LiNiB polytypes and their and high-temperature polymorph *HT*-LiNiB can be represented as stacking of almost planar [NiB] layers alternating with Li layers, however the topology of each layer is different between the *RT*- and *HT*-polymorphs (Figures 3-4). The [NiB] layers are composed of fused distorted nickel hexagons Ni_6B_2 (highlighted in yellow in Figure 4) centered by B-B pairs. In the case of *RT(m)*-LiNiB and *RT(o)*-LiNiB (Figure 3), the structure of [NiB] layer is the same, the difference stems from different stacking sequence of [NiB] layers (AAAA sequence along *a*-axis in *RT(m)*-LiNiB and AABB sequence along *c*-axis in *RT(o)*-LiNiB). Another difference is in arrangement of Li atoms within the layer: a hexagonal pattern in *RT(m)*-LiNiB and a rectangular pattern in *RT(o)*-LiNiB, with the reasonable Li-Li distances of 2.86-3.08 Å and 2.39-3.08 Å, respectively. The structure of *RT*-LiNiB is most likely an intergrowth of two polytypes, as evidenced from high-resolution synchrotron powder X-ray diffraction data (Figure S5-S6).

At higher temperature *RT*-LiNiB transforms to its high-temperature polymorph *HT*-LiNiB. Both polymorphs have layered structures with alternating [NiB] and Li layers, however the structure of the [NiB] layer is different in the type of connectivity between Ni_6B_2 units (Figure 4 *c*-d). In case of *RT(m)*-LiNiB, these Ni_6B_2 units are connected via a common short edge to form chains, which are further fused into [NiB] planar layers (Figure 4*c*). Those layers are further stacked, so there is no any shift between them (Figure 3*d*). The nearly planar [NiB] layers in *HT*-LiNiB, on the other hand, are composed of fused zig-zag chains of the Ni_6B_2 units, and the [NiB] layers are further stacked with a relative shift diagonally by ~ 1/4×1/4 of the unit cell (Figure 4).

The [NiB] planar layers in *HT*-LiNiB ($P2_1/m$) are stacked along the two-fold screw axes 2_1 running along *b*-axis, while in case of *RT(m)*-LiNiB ($P2_1/c$) the stacking direction is perpendicular to the 2_1 screw axis, *e.g.* along a-axis. The observed rearrangement of the layers is most likely driven by the changes in the Li layer, which features hexagonal type packing in *RT(m)*-LiNiB and squared type of packing in *HT*-LiNiB (Figure 4 e-f).

The structures of the layered LiNiB compounds are related to the structures of other Li-Ni-B phases, particularly Ni2B and $LiNi_3B_{1.8}$.[8], [10] The Ni_6B_2 unit is found in the structure of binary Ni_2B boride ($CuAl_2$ structure type, Figure S8), while the Li-layer is similar to that in Li metal (at room temperature cubic-Li has the structure of W, while hexagonal-Li is isostructural to Mg at low temperatures, Figure S8).[8] Furthermore, the $LiNi_3B_{1.8}$ compound[10] can be considered as intermediate link between the family of Li-rich nickel borides and binary Ni_2B. Its crystal structure (idealized structure with no split positions is considered) can be represented as similar [NiB] layers, formed by Ni_6B_2 units alternating with [Li-Ni-B] layers (Figure S8).

The layered structures of the LiNiB polymorphs are unique among the reported compounds in *A*-*T*-B ternary systems (*A* = element of group 1-2, *T* = transition metal of group 4-12).[8] There are a few examples of ternary borides structures, where similar structural units can be singled out (Figure S9): MgRhB ($P6_222$),[14a] $NaPt_3B$ (*P*6/*mmm*)[14b] and $Ba(Sr)_{0.67}Pt_3B_2$ ($P6_3/mmc$).[14c] Interestingly, in case of equiatomic MgRhB, Mg atoms do not occupy one of the layer completely, but replace two out of six Rh atoms in Rh_6B_2 units. Unlike LiNiB, B atoms in the structures of $NaPt_3B$ and $Ba(Sr)_{0.67}Pt_3B_2$ do not form pairs.

Scanning transmission electron microscopy. The commonly used methods to confirm the composition of the lithium nickel borides, such as EDXS or WDXS, are not applicable, since Li and B are below the threshold of the detection limit. The plate-like morphology of the *RT*-LiNiB crystals in SEM images is consistent with layered crystal structures (Figure S10). Qualitative EDXS analysis allowed confirms the presence of Ni, and the absence of any other heavy elements, like Ta from the reaction vessel.

High angle annular dark field (HAADF) scanning transmission electron microscopy (STEM) combined with electron energy loss spectroscopy (EELS) was used to confirm the composition. The crystal in Figure 5 has a layered structure and the stacked-plates character causes the surface layer (that sticks out at the top from the rest of the stack) to appear much thinner that the bulk of the crystal. In this thin part Li, Ni and B signal can be detected on the EEL spectra; no oxygen or carbon signal is present. In the thicker part, the Li and B signal drops drastically due to absorption and only the Ni signal can still be clearly detected.

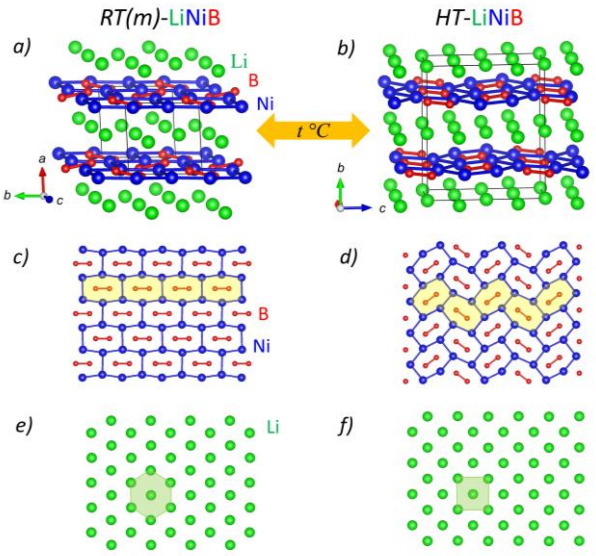

Figure 4. Layered structures of the *RT(m)*-LiNiB (left) and *HT*-LiNiB (right) compounds built from alternating Li- and [NiB]-layers. Different structure of [NiB] and Li layers in two polymorphs is emphasized by highlighting different motif of fused Ni_6B_2 units in yellow (*c* and *d*) and in green for Li layer (*e* and *f*).

The majority of the analyzed crystals had a thick coating, which was determined to be lithium oxide (Figure S11) and hampered the atomic resolution imaging. Overview HAADF STEM images of both *RT*-LiNiB and *HT*-LiNiB indicate that they have a layered structure with an interlayer distance close to 4.4 Å, consistent with the structure models (Figure 6 *a*-*b*). The bright dots on the images correspond to the Ni atomic columns; Li and B columns cannot be seen. The bright stripes (indicated by arrowheads) correspond to blocks where Li-layers are missing. Such slabs are randomly distributed and have a zigzag arrangement of the projected Ni columns (single, double or multiple; Figure 6c). Thus, STEM studies confirmed the layered structures of both LiNiB polymorphs and indicate that Li can be deintercalated leading to doubled or tripled [NiB] layers.

Solid-state NMR Spectroscopy. ^{7}Li and ^{11}B magic angle spinning (MAS) solid-state NMR further shed light on the Li and B coordination environment in *RT*-LiNiB and *HT*-LiNiB structures (Figure 7). The MAS ^{7}Li NMR spectra of the *RT*-LiNiB has two peaks: a major one at ~ 80 ppm and a minor one at ~ 0 ppm. The peak at 0 ppm is most likely originates from diamagnetic impurity phases, such as Li_2O (2.8 ppm), $LiOH{\cdot}H_2O$ (0.4 ppm), or or LiOH (1.3 ppm).[10] The peak at ~80 ppm is attributed to

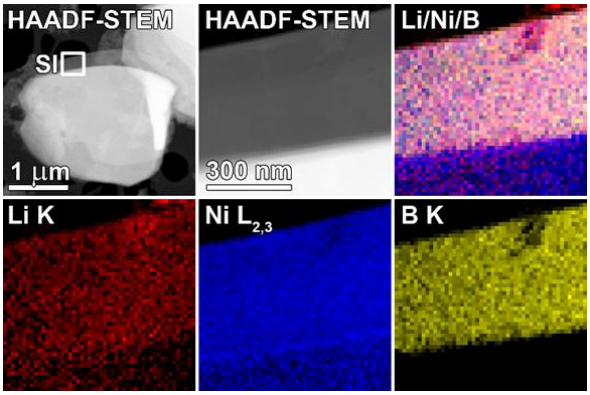

Figure 5. HAADF STEM image of the *HT*-LiNiB crystal with a spectrum image (SI) region indicated by the white square; HAADF signal, mixed Li/Ni/B and individual EELS elemental maps . Li and B signal drops drastically due to absorption in the thicker part of the crystal.

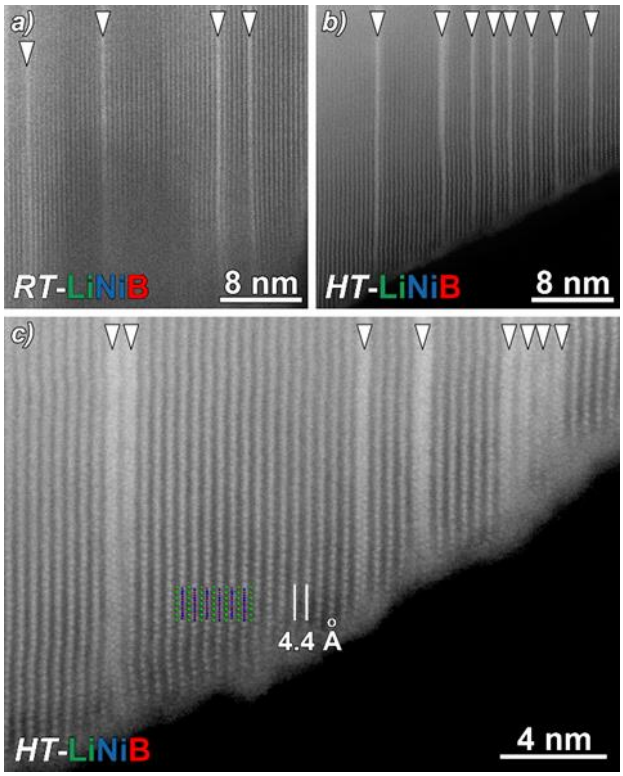

Figure 6. HAADF STEM images of *RT*-LiNiB (*a*) and *HT*-LiNiB (*b*) confirming the layered structures with randomly occurring defects (indicated by arrowheads). Atomic resolution HAADF STEM image of *HT*-LiNiB (*c*) showing the zigzag arrangement of the projected Ni columns in these slabs due to the Li deintercalation.

the *RT*-LiNiB phase and is consistent with the single Li site (*RT(m)*-LiNiB), while the broadness of the peak can be a result of the complexity of the real structure of *RT*-LiNiB, associated with co-existence of several stacking variants of the [NiB] layers, and thus leading to a distribution of similar local ^{7}Li environments and chemical shifts. The chemical shift of ~ 80 pm is shifted to higher frequencies compared to the diamagnetic materials, indicative of Knight shift from conduction electrons,[15] and thus metallic behavior of the *RT*-LiNiB phase. The chemical shift of 80 ppm is slightly higher than ~28 ppm ^{7}Li chemical shift observed for the $LiNi_3B_{1.8}$ phase, but within the range of shifts observed for other Li-containing intermetallics.[10]

The MAS ^{7}Li NMR spectrum of *HT*-LiNiB is distinct from *RT*-LiNiB. There are two ^{7}Li peaks with 2:1.9 ratio at ~ 55-65 ppm and two peaks at ~ 95 and 110 ppm with 1.7:1 ratio, and additionally there is a peak at ~ 0 ppm (Figures 7 and S12). The peak at ~0 ppm was attributed to the diamagnetic oxide/hydroxide impurity, since its intensity considerably decreases upon washing of the sample with water in the nearly anaerobic conditions (Figure S12). Thus, ^{7}Li peaks in the range of 55-110 ppm belong to *HT*-LiNiB phase. These chemical shifts are indicative of Knight shift[58] from conduction electrons,[15] and metallic behavior of the *HT*-LiNiB phase, similar to *RT*-polymorph. A ^{7}Li-^{7}Li EXSY correlation spectrum obtained with a short exchange time of 500 μs confirms that all of the high-frequency lithium signals are associated with the *HT*-LiNiB phase (Figure 7, right). The presence of the off-diagonal peaks in the range of 50-110 ppm suggests that all Li atoms are mobile and diffuse within the Li layer of the *HT*-LiNiB phase. Three peaks are expected for *HT*-LiNiB, based on the structure with three Li sites (2*a*, 2*c*, 4*f*, in $P2_1/m$). STEM images also indicate defects associated with partial Li deintercalation. This together with splitting of some of the peaks in PXRD patterns (Figure S7) point out at additional level of structural complexity in the case of *HT*-LiNiB phase, which could explain the appearance of additional ^{7}Li NMR signals.

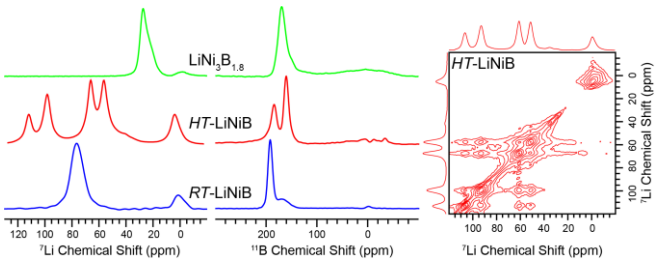

Figure 7. Left: MAS ^{7}Li and ^{11}B MAS solid-state NMR spectra of (top, green trace) hexagonal $LiNi_3B_{1.8}$ phase[29], (middle, red trace) *HT*-LiNiB sample washed with water, and (bottom, blue trace) *RT*-LiNiB phase; Right: 2D ^{7}Li-^{7}Li EXSY correlation spectrum of *HT*-LiNiB showing chemical exchange between different lithium environments. All spectra were obtained with B_0 = 9.4 T and a 25 kHz MAS frequency.

The ^{11}B solid-state NMR for *RT*-LiNiB and *HT*-LiNiB is consistent with their metallic behavior, and the range of ^{11}B chemical shift of 150-220 ppm is similar to the 170 ppm chemical shift observed for $LiNi_3B_{1.8}$ as well as for other metallic borides and borocarbides.[29] Boron atoms in both *RT*- and *HT*-LiNiB form pairs, which are further surrounded by 6 Ni atoms (Figure 3-4). Consistent with the proposed structural models of *RT*-LiNiB, only a single ^{11}B NMR signal is observed. The spectrum of *HT*-LiNiB shows two peaks ^{11}B NMR signals, both with shifts similar to that of *RT*-LiNiB. The differences in topology of the [NiB] layers in *RT*-LiNiB and *HT*-LiNiB as well as the difference in boron coordination by Li likely explain the variation of ^{11}B shifts observed in the solid-state NMR spectra. However, two ^{11}B NMR signals are observed for *HT*-

LiNiB, while only one is expected based upon the crystal structure. The additional ^{11}B NMR signal could arise from boride units that are near to stacking faults, which STEM images indicate are much more numerous in *HT*-LiNiB than *RT*-LiNiB.

Magnetic properties. Temperature dependence of the molar magnetic susceptibility in the range 5-300 K and the field dependence of the magnetization at 5 and 300 K of the *RT*-LiNiB and *HT*-LiNiB phases (Figure S13). Neither superconductivity nor magnetic ordering was observed down to 5 K. Both compounds exhibit temperature-independent Pauli paramagnetism over the entire temperature range, with a susceptibility of ~ 2×10^{-4} emu·mol^{-1}. The field dependence of the magnetization at 5 and 300 K shows a linear dependence with no tendency for saturation, consistent with temperature independent paramagnetism.

Electronic and phonon structure. Phonon spectra were calculated to investigate their dynamical stability (Figure 8). No imaginary phonon frequencies were calculated for the *RT(m)*-LiNiB polytype ($P2_1/c$), indicating that this structure is dynamically stable. However, in the case of *RT(o)*-LiNiB polytype ($Cmc2_1$) and *HT*-LiNiB ($P2_1/m$), negative phonon modes are observed (Figure 8 *b-c*, Table S10). The imaginary phonon modes may lead to new stable structures through atomic displacements and lattice deformation along the eigenvector of the corresponding soft mode.[16] Two negative phonon modes for *RT(o)*-LiNiB polytype ($Cmc2_1$) only involve the motion of Li atoms (Figure 9*a-b*), following which the rectangular lattice of Li will transform into a closed packed hexagonal lattice, similar to the Li layer in *RT(m)*-LiNiB ($P2_1/c$). Our structure relaxation confirms this pathway and the new structures obtained thereafter (Figure 9 *c-d*) have the same stacking variant of [NiB] layers as in *RT(o)*-LiNiB, while the Li layer is the same as in *RT(m)*-LiNiB polytype. These newly generated structures can be thought as an intergrowth variant of two polytpes of *RT*-LiNiB, suggesting that the actual structure of this compound is a complex intergrowth of different stackings of [NiB] layer with additional variation within Li layer. By contrast, in the *HT*-LiNiB the negative phonon modes are originated from the relative motions of Li and [NiB] layers.

RT(m)-LiNiB, *RT(o)*-LiNiB, and *HT*-LiNiB are predicted to be metallic (Figure S14-S15), which is in consistent with NMR Knight shifts and temperature independent Pauli paramagnetism. The Ni atomic orbitals have major contribution to the states right below Fermi level for all Li-Ni-B structures. Bader charge analysis[17] shows that more electropositive Li atoms donating electrons to Ni and B atoms, $Li^{+0.84}[NiB]^{-0.84}$ (Table S10). In contrast, similar analysis performed for $LiCoO_2$ resulted in $Li^{+0.90}Co^{+1.24}(O^{-1.07})_2$ (Table S10). The formal oxidation state of transition metal is different, while the degree of Li ionization is similar in LiNiB and $LiCoO_2$, indicating high mobility of Li in LiNiB similar to that in $LiCoO_2$.

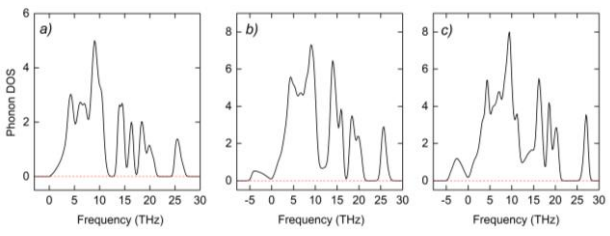

Figure 8. Phonon density of states: *a*) *RT(m)*-LiNiB ($P2_1/c$), *b*) *RT(o)*-LiNiB ($Cmc2_1$), *c*) *HT*-LiNiB ($P2_1/m$).

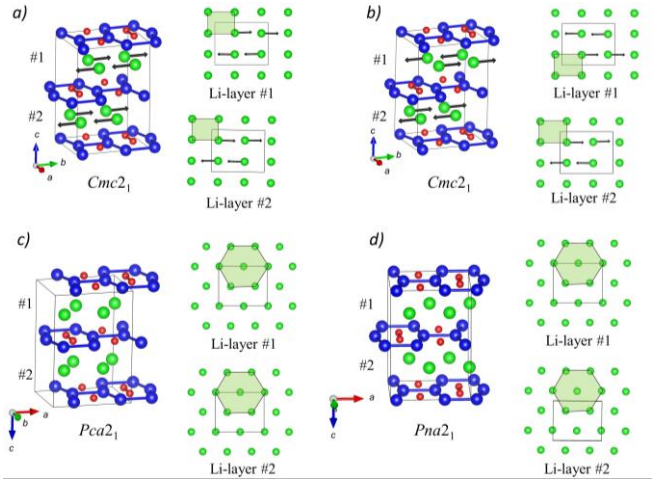

Figure 9. *a*), *b*) atomic displacements of the two negative phonon modes of *RT(o)*-LiNiB ($Cmc2_1$). *c*), *d*) new structures derived from structure of *RT(o)*-LiNiB by following the atomic displacements of the negative phonons plotted in a) and b) respectively. The structure in c) has a space group of $Pca2_1$ (#29) and the formation energy of it is 20 meV/atom lower than in *RT(o)*-LiNiB, while the structure in *d*) has a space group of $Pna2_1$ (#33) and formation energy of it is 19 meV/atom lower than in *RT(o)*-LiNiB.

The newly synthesized LiNiB polymorphs with the unique layered structures and labile Li^+ cations in interlayer spacing can be considered as suitable precursors for further exfoliation/cation extraction to produce single layer 2D transition metal brodie MBenes assemblies, as well as testing those materials as anodes for Li ion battery applications. The hydride route and quenching to room temperatures enables the high-yield synthesis of both polymorphs, thus allowing for further studies of the differences in the atomic arrangement of [NiB] layer on the chosen property in this new class of the exfoliated 2D MBenes. Chemical modification (doping) of the nickel sublattice by another transition metal ion will allow to study confinement of the magnetic moments in highly anisotropic layered structures and 2D assemblies, while further structural and electronic tunability can be realized via aliovalent and ambivalent substitutions in the Li and B sublattices. Further systematic search for new layered boride of alkali and transition metal using hydride route in combination with adaptive genetic algorithm (AGA) crystal structure search is of interest. Moreover, the incorporation of molecular groups into Li spacer layers *via* soft chemistry routes holds promise for discovering new families of compounds with superior properties, as it was demonstrated by the enhancement of the superconducting transition temperature of FeSe by intercalation of a molecular spacer layer.[19]

Conclusion

A family of Li-rich nickel boride polymorphs *RT*-LiNiB and *HT*-LiNiB featuring novel layered structures has been theoretically

predicted using the adaptive genetic algorithm (AGA) and further synthesized utilizing salt-like LiH precursor. Structures of these polymorphs feature alternating Li layers and nearly planar [NiB] layers with unique topology. Within the [NiB] layer, Ni deformed hexagons centered by B-B pairs are further fused to form layers of different topology as seen in *RT*-LiNiB and *HT*-LiNiB, the latter can only be stabilized by quenching from high temperatures. The complex crystal structures of these compounds were studied by combination of single crystal/synchrotron powder X-ray diffraction data, solid-state ^{7}Li and ^{11}B NMR, and scanning transmission electron microscopy. The oxidation and deintercalation processes as a route of further modification of layered LiNiB structures will be of particular interest and is a subject of further investigation, as well as further exploration of Li-rich region of the Li-Ni-B ternary system.

Experimental Section

Experimental Details are provided in the Supporting Information.

Acknowledgements

Financial support from the Iowa State University is gratefully acknowledged. A.J.R, S.L.C., M.P.H. (NMR spectroscopy), P.C.C (magnetization measurement) were supported by the U.S. Department of Energy (DOE), Office of Science, Basic Energy Sciences, Materials Science and Engineering Division. R.A.R. was funded by the Gordon and Betty Moore Foundation's EPiQS Initiative through Grant GBMF4411. The Ames Laboratory is operated for the U.S. Department of Energy by Iowa State University under contract #DE-AC02-07CH11358. Use of the Advanced Photon Source at Argonne National Laboratory was supported by the U. S. Department of Energy, Office of Science, Office of Basic Energy Sciences, under Contract No. DE-AC02-06CH11357.

Keywords: 2D materials • hydride • layered compounds • lithium • transition metal

[1] a) R. Gautier, X. Zhang, L. Hu, L. Yu, Y. Lin, T.O.L. Sunde, D. Chon, K.R. Poeppelmeier, A. Zunger, *Nat. Chem*. **2015**, *7*, 308; b) K. Ryan, J. Lengyel, M. Shatruk, M. *J. Am. Chem. Soc.* **2018**, *140*, 10158; c) A. O. Oliynyk, E. Antono, T. D. Sparks, L. Ghadbeigi, M.W. Gaultois, B. Meredig, A. Mar, *Chem. Mater.* **2016**, *28*, 7324; d) C.C. Fischer, K.J. Tibbetts, D. Morgan, G. Ceder. *Nat. Mater*. **2006**, *5*, 641; e) D.W. Davies, K.T. Butler, J.M. Skelton, C. Xie, A.R. Oganov, A. Walsh, *Chem. Sci.* **2018**, *9*, 1022; f) P. Raccuglia, K.C. Elbert, P.D.F. Adler, C. Falk, M.B. Wenny, A. Mollo, M. Zeller, S.A. Friedler, J. Schrier, A.J. Norquist, *Nature* **2016**, *533*, 73.

[2] X. Zhao, M.C. Nguyen, W.Y. Zhang, C.Z. Wang, M.J. Kramer, D.J. Sellmyer, X.Z. Li, F. Zhang, L.Q. Ke, V.P. Antropov, K.M. Ho, *Phys. Rev. Lett.* **2014**, *112*, 045502.

[3] a) M. Jansen, J.C. Schön, *Angew. Chem. Int. Ed.* **2006**, *45*, 3406; b) M. Jansen, *Angew. Chem. Int. Ed*. **2002**, *41*, 3746; c) M. Jansen, *Adv. Mater.* **2015**, *27*, 3229; d) K. Alberi, *et. al*., J. *Phys. D: Appl. Phys.* **2019**, *52*, 013001.

[4] a) G. Akopov, M.T. Yeung, R.B. Kaner, *Adv. Mater*. **2017**, *29*, 1604506; b) B. Albert, H. Hillebrecht, *Angew. Chem. Int. Ed.* **2009**, *48*, 8640; c) B.P.T. Fokwa, Borides: Solid-State Chemistry. *Encyclopedia of Inorganic and Bioinorganic Chemistry*, **John Wiley & Sons**, Inc. 2014, 1–14; d) H. Park, A. Encinas, J.P. Scheifers, Y. Zhang, B.P.T. Fokwa, *Angew. Chem. Int. Ed.* **2017**, 56, 5575.

[5] a) M. Naguib, M. Kurtoglu, V. Presser, J. Lu, J. Niu, M. Heon, L. Hultman, Y. Gogotsi, M.W. Barsoum, *Adv. Mater*. **2011**, *23*, 4248; b) M. Alhabeb, K. Maleski, B. Anasori, P. Lelyukh, L. Clark, S. Sin, Y. Gogotsi, *Chem. Mater.* **2017**, *29*, 7633.

[6] a) Z. Jiang, P. Wang, X. Jiang, J. Zhao, *Nanoscale Horiz.* **2018**, *3*, 335; b) Z. Guo, J. Zhou, Z. Sun, *J. Mater. Chem. A* **2017**, *5*, 23530; c) T. Bo, P.-F. Liu, J. Zhang, F. Wang, B.-T. Wang, *Phys. Chem. Chem. Phys.* **2019**, *21*, 5178; d) G. Yuan, T. Bo, X. Qi, P.-F. Liu, Z. Huang, B.-T. Wang, *Appl. Surf. Sci.* **2019**, *480*, 448.

[7] a) H. Nishino, T. Fujita, N. Thanh Cuong, S. Tominaka, M. Miyauchi, S. Iimura, A. Hirata, N. Umezawa, S. Okada, E. Nishibori, A. Fujino, T. Fujimori, S. Ito, J. Nakamura, H. Hosono, T. Kondo, T. *J. Am. Chem. Soc*. **2017**, *139*, 13761; b) L.T. Alameda, P. Moradifar, Z.P. Metzger, N. Alem, R.E. Schaak, *J. Am. Chem. Soc*. **2018**, *140*, 8833; c) J. Wang, T.N. Ye, Y. Gong, J. Wu, N. Miao, T. Tada, Hosono, H. *Nat. Commun*. **2019**, 10, 2284.

[8] Inorganic Crystal Structure Database (Web Access), Version 4.2.0; Fachinformationszentrum Karlsruhe: Germany, **2019**.

[9] a) W. Jung, *Naturwissenschaften* **1976**, *63*, 246; b) W. Jung, *Z. Kristallogr.* **1980**, *151*, 113; c) Jung, W. *Z. Naturforsch*. **1977**, *32b*, 1371.

[10] V. Gvozdetskyi, M.P. Hanrahan, R.A. Ribeiro, T. Kim, L. Zhou, A.J. Rossini, P.C. Canfield; J.V. Zaikina, *Chem. Eur. J.* **2019**, *25*, 4123.

[11] a) T. Cox, V. Gvozdetskyi, B. Owens-Baird, J.V. Zaikina, *Chem. Mater*. **2018**, *30*, 8707–8715; b) V. Gvozdetskyi, B. Owens-Baird, S. Hong, J.V. Zaikina, *Materials* **2019**, *30*, 2; c) X. Ma, F. Xu, T.M. Atkins, A.M. Goforth, D. Neiner, A. Navrotsky, S.M. Kauzlarich, *Dalton Trans.* **2009**, 0, 10250; d) J.V. Zaikina, M. Batuk, A.M. Abakumov, A. Navrotsky, S.M. Kauzlarich, *J. Am. Chem. Soc.* **2014**, *136*, 16932; e) F. Sui, S.M. Kauzlarich, *Chem. Mater*. **2016**, *28*, 3099; f) J.V. Zaikina, M.Y. Kwong, B. Baccam, S.M. Kauzlarich, *Chem. Mater*. **2018**, *30*, 8883; g) C.J. Perez, V.J. Bates, S.M. Kauzlarich, *Inorg. Chem.* **2019**, *58*, 1442.

[12] M. Ji, K. Umemoto, C.-Z. Wang, K.-M. Ho, R.M. Wentzcovitch, *Phys. Rev. B* **2011**, *84*, 220105; b) S.Q. Wu, M. Ji, C.-Z. Wang, M.C. Nguyen, X. Zhao, K. Umemoto, R.M. Wentzcovitch, K.-M. Ho, *J. Phys. Condens. Matter*. **2014**, *26*, 035402.

[13] V. Favre-Nicolin, R. Cerny, *J. Appl. Cryst.* **2002**, *35*, 734.

[14] a) A.M. Alekseeva, A. M. Abakumov, A. Leithe Jasper, W. Schnelle, Yu. Prots', J. Hadermann, G. van Tendeloo, E.V. Antipov, Yu. Grin, *Z. Anorg. Allg. Chem*. **2005**, *631*, 1047; b) R. Mirgel, W. Jung, *J. Less-Common Met.* **1988**, *144*, 87–99; c) R.N. Shelton, *J. Less-Common Met.* **1978**, 62, 191.

[15] W.D. Knight, *Phys. Rev.* **1949**, *76*, 1259.

[16] A. Togo, I. Tanaka, I. *Scr. Mater.* **2015**, *108*, 1.

[17] a) W. Tang, E. Sanville, G.J. Henkelman, *J. Phys: Condens. Matter.* **2009**, *21*, 084204; b) E. Sanville, S.D. Kenny, R. Smith, G. Henkelman, *J. Comp. Chem.* **2007**, *28*, 899.

[18] K. Mizushima, P.C. Jones, P.J. Wiseman, J.B. Goodenough, *Mat. Res. Bull.* **1980**, *15*, 783.

[19] M. Burrard-Lucas, D.G. Free, S.J. Sedlmaier, J.D. Wright, S.J. Cassidy, Y. Hara, A.J. Corkett, T. Lancaster, P.J. Baker, S.J. Blundell, S.J. Clarke, *Nature. Mat.* **2013**, *12*, 15.